Title

Molecular Basis of Iterative C–H Oxidation by TamI, a Multifunctional P450 Monooxygenase from the Tirandamycin Biosynthetic Pathway

Journal

ACS Catalysis, 10(22)

ISSN

2155-5435

Authors

Newmister, Sean A
Srivastava, Kinshuk Raj
Espinoza, Rosa V
et al.

Publication Date

2020-11-20

DOI

10.1021/acscatal.0c03248

Peer reviewed

HHS Public Access

Author manuscript

ACS Catal. Author manuscript; available in PMC 2021 November 20.

Published in final edited form as:

ACS Catal. 2020 November 20; 10(22): 13445–13454. doi:10.1021/acscatal.0c03248.

Molecular Basis of Iterative C—H Oxidation by TamI, a Multifunctional P450 monooxygenase from the Tirandamycin Biosynthetic Pathway

Sean A. Newmister[1,†], **Kinshuk Raj Srivastava**[1,†,#], **Rosa V. Espinoza**[1,2], **Kersti Caddell Haatveit**[3], **Yogan Khatri**[1], **Rachel M. Martini**[1,#], **Marc Garcia-Borràs**[3,#], **Larissa M. Podust**[4], **K. N. Houk**[3,*], **David. H. Sherman**[1,5,6,7,*]

[1]Life Sciences Institute, University of Michigan, Ann Arbor, MI 48109, USA

[2]Program in Chemical Biology, University of Michigan, Ann Arbor, MI 48109, USA

[3]Department of Chemistry and Biochemistry, University of California Los Angeles, Los Angeles, CA 90095, USA

[4]Skaggs School of Pharmacy and Pharmaceutical Sciences, University of California San Diego, La Jolla, CA 92093, USA

[5]Department of Medicinal Chemistry, University of Michigan, Ann Arbor, MI 48109, USA

[6]Department of Chemistry, University of Michigan, Ann Arbor, MI 48109, USA

[7]Department of Micobiology & Immunology, University of Michigan, Ann Arbor, MI 48109, USA.

Abstract

Biocatalysis offers an expanding and powerful strategy to construct and diversify complex molecules by C—H bond functionalization. Due to their high selectivity, enzymes have become an essential tool for C—H bond functionalization and offer complementary reactivity to small-molecule catalysts. Hemoproteins, particularly cytochromes P450, have proven effective for selective oxidation of unactivated C—H bonds. Previously, we reported the *in vitro* characterization of an oxidative tailoring cascade in which TamI, a multifunctional P450 functions co-dependently with the TamL flavoprotein to catalyze regio- and stereoselective hydroxylations and epoxidation to yield tirandamycin A and tirandamycin B. TamI follows a defined order including 1) C10 hydroxylation, 2) C11/C12 epoxidation, and 3) C18 hydroxylation. Here we

[*]To whom correspondence should be addressed: David H. Sherman: Life Sciences Institute, University of Michigan, Ann Arbor, MI 48109, USA; davidhs@umich.edu; Tel: 734-615-9907; K.N. Houk: University of California Los Angeles, Los Angeles, CA, 90095, USA; houk@chem.ucla.edu; Tel: 310-206-0515.

[#]Present address:

K.R.S. Regional Centre for Biotechnology, Faridabad-Gurgaon Expressway, Faridabad – 121001, Haryana, India

R.M.M. Department of Chemistry, University of Illinois at Urbana–Champaign, Illinois, 61801, United States M.G.B. CompBioLab, Institut de Química Computacional i Catàlisi (IQCC) and Departament de Química, Universitat de Girona, Campus Montilivi, 17071 Girona, Catalonia, Spain

[†]These authors contributed equally to the work

Supporting Information: Crystallographic coordinates and data for TamI substrate free (PDB: 6XA3) and TamI in complex with tirandamycin C (PDB: 6XA2) are available through the Worldwide Protein Data Bank. This information is available free of charge on the ACS Publications website.

Conflict of Interest: The authors declare no competing interests.

present a structural, biochemical, and computational investigation of TamI to understand the molecular basis of its substrate binding, diverse reactivity, and specific reaction sequence. The crystal structure of TamI in complex with tirandamycin C together with molecular dynamics simulations and targeted mutagenesis suggest that hydrophobic interactions with the polyene chain of its natural substrate are critical for molecular recognition. QM calculations and molecular dynamics simulations of TamI with variant substrates provided detailed information on the molecular basis of sequential reactivity, and pattern of regio- and stereo-selectivity in catalyzing the three-step oxidative cascade.

Graphical Abstract

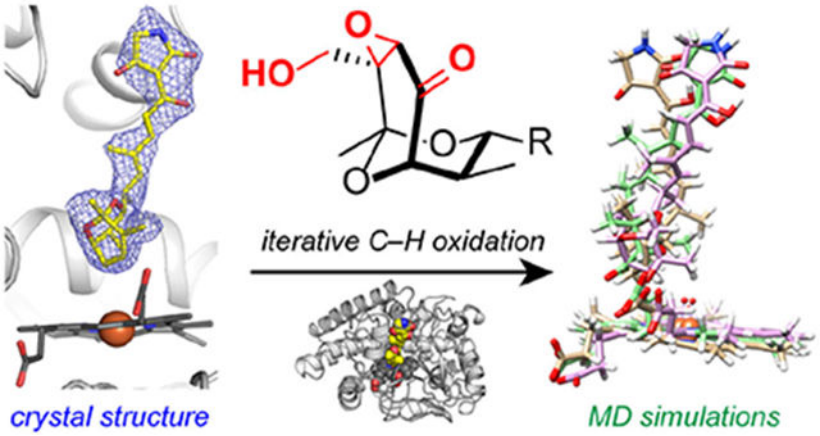

Keywords

natural product; biosynthesis; cytochrome P450; enzyme structure; molecular dynamics; antibiotics

INTRODUCTION

Selective functionalization of C—H bonds to form C—X or C—C bonds is a powerful strategy for the synthesis of complex organic compounds and other high-value chemicals. Although the past decade has seen expansive applications of C—H functionalization for chemical synthesis, controlling regio- and stereoselectivity remains a significant challenge. Most research has focused on catalyst-controlled methods for selectivity in C—H functionalization.[1] While several effective small molecule catalysts have been developed in the past few years, Nature has utilized selective C—H functionalization throughout evolution via enzymemediated catalysis. In various metabolic pathways, enzymes perform diverse C—H functionalization reactions such as halogenation, hydroxylation, alkylation, and amination with high regio- and stereo-selectivity; therefore, biosynthetic enzymes are an excellent resource to access biocatalysts that can be harnessed for efficient C—H functionalization with high selectivity over a broad range of substrates.

Most biological site-selective C—H functionalizations are catalyzed by cytochromes P450 (P450s) with high chemo-, regio-, and stereoselectivities. P450s are found in all domains of

life including viruses,[2] and catalyze a broad range of oxidative transformations such as aliphatic and aromatic bond hydroxylation, double bond epoxidation, C—C bond formation, decarboxylation, desaturation, oxidative rearrangement of carbon skeletons and other transformations.[3] These P450s are frequently integrated into biosynthetic gene clusters and perform oxidative tailoring of complex substrates to produce secondary metabolites.[4] The remarkable versatility of P450s has driven increased applications for synthetic biology[5] and for late-stage functionalization of several natural products including Nigelladine A, Juvenamicins, Vancomycin, Mycinamicin and Thaxtomin D.[6] Taking advantage of inherent evolvability of these P450s, researchers have engineered P450s to catalyze new and non-natural reactions including C-Si, C-B, anti-Markovnikov alkene oxidation for which no enzymes exist in nature.[7-11] The continued discovery, characterization, and engineering of novel biosynthetic P450s provides provides new insights for biocatalyst development and expanding the toolbox for addressing the challenges of C-H functionalization.

TamI, is a multifunctional cytochrome P450 from *Streptomyces* sp. 307-9 that catalyzes late-stage oxidation at three positions on the bicyclic ketal moiety of tirandamycin C (**1**),[12] which is a required modification for bacterial RNA polymerase targeting by the tirandamycins.[13] In distinction from flexible enzymes that act on a variety of substrates, multifunctional P450s catalyze a stepwise sequence of reactions on a particular substrate. This uncommon reactivity has been studied in bacterial enzymes MycG[14] and AurH[15], as well as other fungal[16] and plant[17] P450s. Previously, we reported *in vitro* functional characterization of TamI, and a partner flavin adenine dinucleotide (FAD)-dependent oxidase, TamL, and established their roles in the installation of the C10 keto, C11/C12 epoxide and C18 hydroxyl groups on native substrate **1** (Figure 1).[12] TamI catalyzes initial hydroxylation of **1** at C10, to form tirandamycin E (**2**); subsequently, TamL catalyzes oxidative conversion of C10 hydroxyl to carbonyl to yield tirandamycin D (**3**). Further epoxidation and hydroxylation catalyzed by TamI complete the oxidative catalytic cascade to yield antibiotics tirandamycin A (**4**) and tirandamycin B (**5**), respectively (Figure 1). Despite detailed functional studies, the molecular basis of the iterative nature of TamI remained unexplored, which we were motivated to pursue using structural biology and computational approaches. A key hypothesis that we sought to interrogate was whether TamI uses a discrete substrate binding mechanism in which the tetramic acid moiety anchors **1** in a position appropriate for the iterative oxidation reactions to occur. Substrate anchoring has notably been observed in the TamI homologue PikC (47% sequence identity), where presence of the dimethylamino sugar desosamine or a suitable surrogate drives substrate recognition, thus enabling oxidation of non-native substrate scaffolds bearing this recognition element.[18] Presence of such a feature in TamI could provide additional opportunity for a tetramate-based anchoring strategy for oxidative tailoring of diverse chemical scaffolds.

Here we report the molecular characterization of TamI to understand in detail its structure, substrate molecular recognition, and the basis for its regio- and stereo-selectivities. The TamI structure together with molecular dynamics simulations and subsequent mutagenesis experiments indicate that hydrophobic interactions with the central polyene chain region of **1** is the critical element for substrate recognition and catalysis. QM calculations, together with

molecular dynamics simulations, provide detailed information on the molecular basis of regio- and stereo-selectivity.

RESULTS AND DISCUSSION

Structural analysis of TamI in complex with tirandamycin C

The structure of TamI in complex with **1** was solved by molecular replacement at 2.7 Å resolution using the ligand free structure as a search model (Figure S1-S2). The overall structure exhibits the characteristic P450 fold with a single heme cofactor covalently bound via a Cys359 heme-thiolate (Figure 2A). The asymmetric unit is composed of eight unique chains which are differentiated by their crystal packing environment and show high conformational similarity (r.m.s. deviations < 0.3 Å) (Figure S3); therefore the best-ordered chain (chain A, average Bfactor 50 $Å^2$) was used for analysis and interpretation. Structural homology analysis revealed CYP267B1 (6GK5), CYP154C5 (4J6C), CYP245A1 (2Z3U), and CreJ (5GWE) as the closest structural homologs with an average r.m.s. deviation of 2.1 Å (DALI).[19] These enzymes are involved in oxidation of medium chain fatty acids, steroids, alkaloids, alkylphenols.[20-23]

Tirandamycin C is unambiguously bound in the active site with well-defined electron density for the entire molecule (Figure 2B). The bound substrate is enveloped completely within the enzyme without evidence of direct access to bulk solvent. Tirandamycin C makes close contacts with the enzyme throughout its structure (Figure 2B). The tetramic acid moiety is bound in a pocket composed of segments of four distinct loop regions of the protein: the β1-1/2 loop (residues Val42, Pro43, Val44), the BC loop (Phe92), the FG loop (Val185), and the β3-3/2 loop (Ser 397, Thr398, Leu399) (Figure 3A). Tetramic acid binding is mediated by several direct polar interactions via the carbonyl oxygen of Pro43, the amide nitrogen of Thr398 and Leu399, and the side chain hydroxyls of Ser397 and Thr398, and by hydrophobic contacts with the side chains of Val44 and Phe92 (Figure 3A).

In addition to the tetramic acid component of the substrate there are several interactions along the length of the polyene chain and the bicyclic ketal. The linear polyene predominantly contacts residues from the β3-3/2 loop region (Leu399 and Ile400),FG region (Val185) and BC loop (Phe92). These hydrophobic side chains constrict the binding site in this region and lead to a hydrophobic pocket adjacent to the heme center in which the bicyclic ketal is bound. Numerous hydrophobic side chains line the binding site of the bicyclic ketal (Leu101, Leu244, Leu295) in addition to other non-polar residues His102, Gly248, Thr252 and Thr299 (Figure 4A). Consistent with the observed order of oxidation by TamI in which C10 is first hydroxylated to form **2**, the C10 atom distance to the heme-iron is 4.1 Å, which is suitable for hydroxylation upon redox partner binding and iron-oxo formation. The conserved I-helix residues Glu250 and Thr251, which have been implicated in proton delivery during dioxygen activation[24] are also found in this region adjacent to the bicyclic ketal moiety.

Mutagenesis and biochemical characterization to probe the molecular basis of substrate binding and anchoring mechanisms

Based on the PikC crystal structure in which a salt-bridge interaction distal from the site of oxidation provided substrate anchoring,[18, 25-26] we sought to investigate whether the tetramic acid moiety of **1** could have an analogous role in TamI. Numerous polar interactions about the tetramic acid moiety in the TamI active site appear consistent with a mechanism that permits iterative oxidation of the distal bicyclic ketal, which we probed experimentally and computationally (see below). Mutagenesis of TamI active site residues in proximity to **1** was performed to assess their specific roles in catalysis. TamI mutant assays were conducted using an optimized three component system composed of TamI, spinach ferredoxin and ferredoxin reductase. To probe whether the dienoyl tetramic acid moiety of the native substrate **1** plays a role in substrate anchoring, we performed mutagenesis of active site residues Ser397, Thr398, Pro43, Val44, and Val185 (Figure 3). Based on the complex structure, we hypothesized that the polar interactions mediated by the side chain hydroxyl groups of Ser397 and Thr398 could be required for proper substrate binding and perhaps could act as a substrate anchor similar to the desosamine sugar of narbomycin/YC-17 and Asp50/Glu85 in PikC.[18, 25-26] Therefore, we prepared single (S397A, T398A, V185A) and double (P43A/V44A) amino acid variants. Analysis of these mutants, however, revealed no evident changes in product profile or abundance compared to wild type TamI in an end-point assay. Furthermore, these variants showed minor perturbations in K_d measured by UV spectral assay where addition of substrate was used to displace the axial water ligand (Table S2, Figure S4). This demonstrated that these polar side chain interactions near the dienoyl tetramic acid moiety have no direct influence on the TamI-mediated TirC to TirE conversion and refuted a tetramic acid based anchoring mechanism. Considering the array of backbone mediated interactions with the tetramic acid moiety, and also the numerous close contacts along the full substrate molecule, we expanded our analysis to alternative active site interactions with bound **1**.

Thus, we examined a cluster of hydrophobic and aromatic residues (Leu399, Ile400, Phe92) located near the polyene region of the substrate. Substitution of Phe92 with alanine resulted in complete loss of catalytic activity in an end-point assay. The double mutant L399A/I400A demonstrated significantly reduced activity (Figure 3B). In these cases, the spectrophotometric assay showed no shift for these mutants (Figure S5) likely indicating perturbed substrate binding. These data indicated that the aromatic and hydrophobic residues surrounding the substrate are critical for C-10 hydroxylation.

Finally, we probed the active site residues (Leu101, His102, Leu295, Thr299) proximal to the bicyclic ketal moiety for their role in substrate binding and product profile. We created a double mutant (L101V/H102S) to examine the impact of increasing the active site volume. However, we did not observe any change in product profile that would indicate relaxed site selectivity for the first oxidation event; instead we observed a significant decrease in TirC to TirE conversion. Presumably, the Leu101 and His102 side chains are important for substrate binding through interactions with the C14 methyl group, which is evident in the crystal structure. Specifically, the Cδ atom of Leu101 is at ~3.4 Å, Nε of His102 is at ~4 Å in relation to the oxygen atoms of bicyclic ketal moiety in **1**. These interactions may be

required for proper positioning of the bicyclic moiety with respect to heme-iron for C10 hydroxylation. We also generated alanine substitutions at Leu295 and Thr299, which are located on the opposite side of the active site and in proximity of the bicyclic ketal moiety. However, this TamI double mutant displayed wild type activity in its ability to convert substrate to **2** (Figure 4).

In summary, mutagenesis studies revealed that the hydrophobic residues in proximity to substrate **1** (Leu399, Ile400, Phe92) are essential for C-10 hydroxylation. These data further suggested that the polyene chain of tirandamycin substrates are a critical component and that appropriate substrate orientation is achieved through hydrophobic and steric interactions with non-polar residues (Leu399, Ile400) and the aromatic ring of Phe92.

Computational investigation of regio- and stereo-selectivity for sequential reactivity and pattern of oxidation

A notable feature of the TamI enzyme is its ability to selectively oxidize multiple positions of tirandamycins in a specific and sequential manner. We used computational methods of density functional theory (DFT) and molecular dynamics (MD) simulations to characterize the intrinsic reactivity of these competing oxidations on the tirandamycin substrates and classify how the enzyme influences the regio- and stereo-selectivity.

Using a truncated model of the tirandamycins C, D, and A containing the biketal moiety and the reactive Fe(IV)-oxo radical cation, we used DFT methods to calculate the transition state barriers for all the competing oxidations, C10 hydroxylation, C11/12 epoxidation, and C18 hydroxylation (Figure 5A). For the first substrate in the oxidative cascade, **1**, the lowest energy barrier is at the C10 position for allylic hydroxylation with no difference between abstracting the *R* or *S* hydrogen, as they both have C—H abstraction barriers of 14.5 kcal/mol (Figure 5A, Figure S6). This matches the experimentally observed regioselectivity, but it indicates that the active site environment of TamI is essential for distinguishing the selectivity between these diastereomeric transition states. For **3**, the second substrate in the TamI oxidation cascade, the front facing epoxidation at C11/12 is lowest in energy by 1.9 kcal/mol, which matches the experimentally observed stereoselectivity and reaction specificity (Figure 5A, Figure S7). Lastly, we calculated the transition state barriers for the final substrate, **4**, which has a barrier of 17.5 kcal/mol. These calclulated energetic barriers through the oxidation cascade match the trend reported for the TamI-RhFRED fusion protein, where k_{cat} drops significantly (0.11 min^{-1}) for the final oxidation of **4** compared to the first oxidation of **1** (40.5 min^{-1}) or second oxidation of **3** (83.8 min^{-1}).[12] While these energetic trends match the order of sequential reactivity without accounting for the affect of enzyme environment on the activation barriers, we analyzed more of the stereoselectivity and how TamI biases towards the experimentally observed reactions, particularly for the C10 allylic hydroxylation step.

MD simulations were performed to analyze the influence of TamI on the regio- and stereoselectivity within the oxidative cascade. We performed the simulations beginning from the co-crystal structure of **1** with TamI. To ensure these simulations were representative the tautomeric state of the tetramic acid was examined computationally (Figure S8) with the enol tautomer **1** having the lowest relative energy. The distances of key atoms of the **1**

bicyclic ketal (C10-C11-C12-C18) from the reactive Fe(IV)-oxo radical cation were tracked to explore the regioselectivity of the first oxidation event. Both C10 and C11 remained within ~4 Å throughout the 500 ns simulation, consistent with initial C10 hydroxylation (Figure S9). We next analyzed how the enzyme orients the substrate geometry at C10 relative to the Fe(IV)-oxo radical cation, and compared to the ideal transition state geometry calculated with QM. By plotting the O_{heme}–H10 distance and O_{heme}–H–C10 angle for both the *S* and *R* hydrogens relative to that of the ideal transition state geometry we find that TamI controls the orientation of **1** such that the S hydrogen is closer to a transition state geometry for the duration of the simulation (Figure 5B). This suggests that TamI controls the stereoselectivity for this C10 allylic hydroxylation step, which is likely due to the hydrophobic interactions according to the experimental mutational analysis, and is consistent with the isolation of a single C10 stereoisomer from the fermentation broth of *Streptomyces* sp. 307-9. MD simulations were similarly performed on both **3** and **4**, which revealed that the orientation of the tirandamycin substrates change upon increasing oxidation. The geometry of the substrate throughout these simulations, including a dihedral angle for epoxidation of **3** and the angle for C—H abstraction of **4**, were compared those of the ideal transition state geometry (Figure S10), which reveal that the tirandamycins can occupy the appropriate geometry for the expected reactivity in the enzyme active site. This is also demonstrated in visualizing the top occupied clusters of the MD simulations, which when overlayed, show different substrate binding modes as the oxidation cascade progresses and show that the expected reactive position for **3** and **4** (C12 and H18, respectively) to be closest to the reactive Fe(IV)-oxo radical cation in the corresponding simulations (Figure S10).

As reported, mutagenesis experiments highlighted the importance of the hydrophobic residues within TamI's active site: F92, L399, and I400. We analyzed the influence of these residues on the substrate orientation by performing MD simulations of WT TamI with **1**, as well as the single point mutants, F92A, L399A, and I400A. We found that the RMSD of **1** within these various simulations is much lower in the WT relative to the mutants, which shows that the substrate maintains a more stable geometry within the active site. (Figure 5C, Figure S11) However, **1** occupies many different positions in the active sites of the F92A, L399A, and I400A mutants, suggesting that these residues are essential for generating the proper geometry for catalysis.

Lastly the MD simulations provided insight into the binding mode of Tirandamycin C in comparison to other P450s regarding substrate anchoring, which has been a key component of substrate engineering efforts with biocatalytic P450s. Surprisingly the extensive polar interactions about the tetramic acid observed in the crystal structure (Figures 2-3) rapidly relax within the first few ns of the MD simulation (Figure S12), while proximity of the bicyclic ketal to the heme center is maintained. Consistent with the experimental data, this observation also indicates that hydrophobic interactions around the polyene region are most critical for productive substrate binding and catalysis in TamI. These combined biochemical, structural and computational analyses reveal key determinants for binding and catalysis that are distinct from the homologous P450 PikC (47% seq id) in which electrostractic interactions between carboxylate side chains and the desosamine dimethylamino group are

paramount. This was unexpected, given the similarity between the active site architecture and apparent substrate binding mode in the complex structures (Figure 6). Given the work from related macrolide oxidizing P450s MycC1[27] (41% seq id-TamI) and TylH1[28] (35% seq id-TamI) we observe that natural product biosynthetic P450s employ a variety of strategies to accommodate substrate, and that subtle differences can have pronounced functional outcomes. In the case of TylH1, mutation of a few key residues in the BC and FG-loop region were sufficient to convert a "specialist" enzyme with narrow substrate scope into a "generalist" that could accommodate a variety of glycosylated (e.g. macrolide) and non-glycosylated (e.g. macrolactone) substrates reminiscent of its homolog MycC1. Future exploration of substrate scope and protein engineering in TamI will be enabled by the conceptual basis established in this work.

CONCLUSION

The current structural and computational investigation of TamI demonstrated the overall structure, molecular basis of substrate binding and pattern of sequential oxidation of **1**. Comparison of these structures highlights the conformational movement upon substrate binding. The substrate-bound form of TamI adopts a closed state in which **1** is buried inside the protein core consistent with previous reports of substrate-induced conformational changes in P450 enzymes. The tirandamycin C-bound structure of TamI revealed key residues responsible for catalysis. TamI mutational analysis demonstrated that steric and hydrophobic interactions mediated by Phe92, Leu399, Ile400 are critical for **1** oxidation. These experimental observations were further verified by MD simulations of the alanine mutants of Phe92, Leu399, Ile400 in which we observed that the substrate samples diverse binding orientations due to the loss of hydrophobic and **π-π** interactions. Overall, these data reveal the dominance of hydrophobic interactions with the entire substrate for adequate positioning in the active site. QM calculations describe the inherent preference of C10 (secondary allylic carbon) hydroxylation of **1** in the first oxidation step, but displayed no energetic preference for the stereoselectivity in C10 hydroxylation. MD simulations demonstrate that TamI orients the substrate in a specific geometry where the pro-*S* hydrogen is closer to the ferryl oxygen for abstraction. This observation verifies the single stereoisomer isolated from the fermentation broth of *Streptomyces* sp. 307-9. QM calculations provide further insights into the energetic preference for the subsequent reactions in the cascade that match the experimentally observed order of oxidation. MD simulations with **3** and **4**, demonstrated that the substrate binding orientations consistent with idealized geometries are preferred in the active site environment. Together these results provide detailed information on physiochemical principles that control substrate binding, specificity and selectivity of TamI in catalyzing iterative multistep C—H oxidation of tirandamycin intermediates to produce increasingly potent antibiotic molecules.[29] This investigation further underscores the importance of identifying and exploring multi-functional natural product biosynthetic tailoring enzymes that catalyze late stage C—H functionalization of complex organic compounds.

MATERIALS AND METHODS

Materials & general experimental procedures:

Unless otherwise noted, chemicals, reagents, and solvents were purchased from EMD Millipore, Sigma-Aldrich, and Thermo Fisher Scientific. Agarose for gel electrophoresis was purchased from BioExpress (VWR). Kanamycin sulfate, isopropyl-β-Dthiogalactopyranoside (IPTG), and dithiothreitol (DTT) were obtained from Gold Biotechnology. Tris-HCl, ampicillin disodium salt and $NADP^+$ were purchased from Amresco. Chloramphenicol was obtained from Roche. Thiamine and NADPH were purchased from Chem-Impex. δ-aminolevulinic acid was purchased from Oakwood Chemical. Lysozyme was purchased from RPI. Imidazole was purchased from AK Scientific. Amicon Ultra centrifugal filters used for protein concentration were from EMD Millipore. PD-10 columns were purchased from GE Healthcare. Glucose-6-phosphate was from Biosynth, and glucose-6-phosphate dehydrogenase (yeast) was from Alfa Aesar.

Deionized water was obtained from a Milli-Q system (EMD Millipore) using Q-Gard 2/ Quantum Ex Ultrapure organex cartridges. Media components for *E. coli* growth were purchased from EMD Millipore, Sigma-Aldrich, and Thermo Fisher Scientific unless otherwise specified. Glycerol was purchased from BDH (VWR). LB broth (Miller) and LB agar (Miller) were obtained in pre-made granulated form from EMD Millipore. TB broth was made from individually purchased components and consisted of 4% (v/v) glycerol. Media and solutions were autoclaved or sterile filtered before use. For bacterial culture, all media solutions were autoclaved and buffers, and other solutions, pH was monitored using a VWR sympHony SB70P pH meter calibrated according to the manufacturer's specifications. When specified, room temperature (rt) was ~22-23 °C.

DNA oligonucleotides for cloning and mutagenesis were purchased from Integrated DNA Technologies. PCR was performed using a Bio-Rad iCycler thermal cycler system. Restriction endonucleases and other associated molecular biology reagents were purchased from New England Biolabs. Invitrogen PCR cleanup/gel extraction and plasmid miniprep kits were purchased from Thermo Fisher Scientific. All DNA manipulations were accomplished following the manufacturer's protocols. DNA concentrations and protein purity indexes were measured using a NanoDrop ND-1000 spectrophotometer. The DNA sequencing was performed at the University of Michigan DNA Sequencing Core. *E. coli* DH5α was used for plasmid preparation and maintenance while *E. coli* BL21(DE3) was used for protein overexpression. Chemically competent *E. coli* cells were prepared using the method of Inoue.[30] Optical density (OD_{600}) was measured using an Eppendorf BioPhotometer.

Protein purifications were performed manually using prepacked Ni^{2+}–NTA columns with GE peristaltic pump P1, and automatically with GE columns and AKTA Pure FPLC machine, Reverse-phase high-performance liquid chromatography (HPLC) purification was performed using Luna C18 columns with the following specifications: dimensions, 150 x 4.6 mm; particle size, 5 μm; pore size, 100 Å; and a solvent system of acetonitrile and H_2O supplemented with 0.1% formic acid.

All protein figures were generated using Pymol software.

Cloning, site-directed mutagenesis, and preparation of recombinant enzymes:

The *tamI*_pSJ2 expression vector was constructed as described previously.[12] For crystallization, *tamI* was subcloned into a modified pET28 vector containing a TEV-cleavable N-terminal His_8 tag using the "Quikchange" cloning protocol ("*tamI*_pET28H8T"). Site-directed mutagenesis of TamI was performed by PCR using Phusion High-Fidelity DNA Polymerase and a standard site-directed mutagenesis protocol. All constructs and mutations were verified by Sanger DNA sequencing at the University of Michigan DNA Sequencing Core.

Overexpression and purification of TamI and it's recombinant mutant proteins:

Expression and purification of TamI from the *tamI*_pSJ2 expression vector was conducted as described previously.[12] The construct *tamI*_pET28H8T was used to transform *E. coli* BL21(DE3) for protein overexpression. Individual colonies were selected for overnight growth (37 °C) in 10 mL LB containing kanamycin (50 μg/mL). 6 x 1 L of TB (2.8 L Fernbach flasks) supplemented with kanamycin (50 μg/mL), and glycerol (4% v/v) were inoculated with 10 mL overnight cultures and incubated at 37 °C (200 rpm). When the OD_{600} reached 0.6-1.0, the cultures cooled in an ice-water bath (10-20 min) before IPTG (0.2 mM) and δ-aminolevulinic acid (1 mM) were added to induce protein expression and to promote production of the heme cofactor in *E. coli*, respectively. The cultures were grown at 18 °C for 18-20 h before the cells were harvested by centrifugation and stored at −80 °C. The following purification steps were performed on ice or at 4 °C. The cells were thawed and resuspended in 30 mL of lysis buffer (50 mM Tris-HCl, pH 7.4 at room temperature , 50 mM NaCl, 10% (v/v) glycerol, 1 mM PMSF, 0.5 mg/mL lysozyme, 2 mM $MgCl_2$, 5-10 U/mL Benzonase nuclease) per 1 L of original overexpression culture (i.e., 2-3 mL per 1 g of cells). The cell suspension was incubated on a nutating shaker for 1 h prior to sonication using a Model 705 Sonic Dismembrator (Thermo Fisher Scientific) and centrifugation at 50,000 x g for 30 min to remove cellular debris. To the resulting clarified lysate 4 M solutions of NaCl and imidazole were added to final concentrations of 300 mM and 10 mM, respectively. The lysate was filtered through a syringe-operated 0.45 μm filter (Corning) before loading onto a prepacked column containing 7mL of Ni-NTA resin (Qiagen) using peristaltic pumps (GE Healthcare). The loaded material was washed with 5 CV of wash buffer (50 mM Tris-HCl, pH 7.4, 300 mM NaCl, 10 mM imidazole, 10% (v/v) glycerol) followed by 10 CV of wash buffer containing 5% elution buffer (50 mM Tris-HCl, pH 7.4, 300 mM NaCl, 300 mM imidazole, 10% (v/v) glycerol) to remove additional protein contaminants. TamI was eluted with elution buffer and the fractions containing pure material were assessed by SDS-PAGE and by monitoring absorbance A_{420}/A_{280}. Pooled fractions were concentrated using 30 kD MWCO centrifugal filters. Concentrated protein was dialyzed against storage buffer (50 mM Tris, pH 7.4, 1 mM EDTA, 0.2 mM DTT, 10% (v/v) glycerol). Aliquots of purified protein were flash frozen in liquid N_2 and stored at −80 °C. The concentration of functional P450 was assessed by obtaining CO difference spectra according to the established protocol.[31] For crystallization, the His-tag was removed after Ni^{2+}-NTA purification by incubation with purified TEV protease (1: 30 molar ratio) during dialysis in storage buffer overnight. Un-cleaved TamI and the His-tagged TEV were

removed by applying the digest to a Ni^{2+}-NTA column equilibrated with loading buffer. Cleaved TamI was collected in the flow-through fractions and concentrated using an Amicon Millipore concentrator (30 kD MWCO). The concentrated TamI solution was subjected to size exclusion purification via an ÄKTA FPLC system (GE Healthcare) with Superdex 200 Increase 10/300 GL column in storage buffer (50 mM Tris, pH 7.4, 1 mM EDTA, 0.2 mM DTT, 5% (v/v) glycerol). Purified fractions were flash frozen in liquid N2 and stored at −80 °C. To obtain a crystal structure of the TamI•tirandamycin C substrate complex, TamI was incubated overnight with 0.2 mM TirC at 4°C.

The UV–visible spectrum of the purified substrate-free TamI exhibited a major(γ) Soret peak at 417 and the smaller α and β bands at 567 and 533 nm, respectively, indicating that the TamI protein exists in its low spin state. The dithionite reduced spectrum of TamI displayed the absorption maximum of the Soret band at 410 nm. The reduced carbon monoxide bound form of the protein showed a typical peak maximum at 450 nm.

Expression and purification of other proteins:

The plasmid (pMAL-c, New England Biolabs) encoding spinach ferredoxin reductase linked to the C-terminus of *E. coli* maltose-binding protein (MBP) was obtained as a gift from Dr. Giuliana Zanetti. This construct was transformed into *E. coli* BL21(DE3) cells, and proteins were expressed and purified as described previously.[27] Spinach ferredoxin was expressed and purified as noted elsewhere.[32]

Structure of substrate-free TamI:

Initial efforts to determine the TamI crystal structure were conducted using a *tamI*-pSJ2 expression vector containing an N-terminal His_8 tag.[12] Crystals grown with this construct were used to solve the TamI structure by molecular replacement and revealed a single polypeptide chain in the asymmetric unit; however, the P450 active site was occupied by sixteen N-terminal residues of a symmetryrelated protomer (Figure S1). The bound N-terminal segment was derived from the linker region between the His_8 tag and the *EcoR*I restriction site and prompted us to construct a tobacco etch virus protease (TEV)-cleavable construct (*tamI*-pET28H8T) where the affinity tag and linker could be removed by digestion. Crystals of substrate-free TamI were grown by vapor diffusion at 20 °C with a well solution composed of 3.5 M sodium formate, pH 7.0 and 0.1 M strontium chloride. Crystals were harvested using nylon loops and vitrified by rapid plunging into liquid nitrogen. Substrate-free TamI crystallized in space group *I*422 with unit cell dimensions of a = 154.5, b = 154.5, c = 91.8 Å and one chain in the asymmetric unit. X-ray data were collected at 100K on the Advanced Light Source 8.3.1 beamline in Berkeley CA, USA. Diffraction data were integrated and scaled using MOSFLM[33] and SCALA.[34] The structure of TamI was solved by molecular replacement with Phaser-MR[35] using PikC (PDBid: 2X5W, chain B) as a search model. Three rounds of autobuild using Buccaneer[34] were used to provide and initial model. Iterative rounds of manual building in Coot[36] and refinement with Refmac[37] and Phenix.refine[38] were used to furnish the final model. Data collection and refinement statistics are given in Table S2.

Structure of tirandamycin C-bound TamI:

TEV-cleaved TamI in the presence of tirandamycin C gave a different crystal form with eight chains in the asymmetric unit and substrate bound in each active site (Figure 2, Figure S2). Crystals of tirandamycin C-bound TamI were grown by vapor diffusion by mixing 2 μL of 7 mg/mL tirandamycin C-bound TamI with 2 μL of a well solution composed of 1.6 M ammonium sulfate, 0.9 M sodium chloride, 0.1 M bis-tris pH 6.5, 2.5% ethylene glycol. Narrow, rod-shaped crystals were cryoprotected by the addition of well solution containing 9% ethylene glycol. 0.2 mM tirandamycin C, 2% DMSO directly to the sitting droplets. Cyrstals were harvested using nylon loops and vitrified by rapid plunging into liquid nitrogen. Tam•tirandamycin C complex crystallized in spacegroup *C*2 with unit cell dimensions of a = 224.6, b = 57.2, c = 282.7 Å, α = 90°, β = 90.9°, γ = 90° and eight chains in the asymmetric unit. X-ray data were collected at 100 K on beamline 23ID-B at the General Medical Sciences and Cancer Institute Structural Biology Facility at the Advanced Photon Source in Argonne, IL, USA using helical data collection along the long axis of the rod-shaped crystal. Diffraction data were integrated and scaled using XDS.[39] The structure was solved by molecular replacement with Phaser-MR[35] using substrate-free TamI as a search model. To generate the intial model Phenix.autobuild[38] was performed using an eightfold-NCS averaged map. Iterative rounds of manual building in Coot[36] and refinement with Phenix.refine[38] were used to furnish the final model. Data collection and refinement statistics are given in Table S1.

UV-visible absorption spectroscopy:

Measurement of UV-visible spectra for TamI and mutant protein were measured at room temperature on Molecular Devices SpectraMax M5 UV-visible spectrophometer. Proteins were dissolved in 10mM potassium phosphate buffer, pH 7.4, were used for the measurement of spectra of the oxidized and the reduced form of TamI. The mutant proteins were reduced with a few grains of sodium dithionite and the concentration of the active P450 form of TamI was confirmed by CO-difference spectroscopy using ε(450-490) = 91 mM $^{-1}$cm^{-1}. After CO bubbling of the solution for 30-40 s, the spectrum of CO-bound reduced P450 species was recorded using the previously reduced spectrum for the same sample as a reference (Figure S13). The spectral shifts induced by tirandamycin binding were assayed at room temperature under aerobic conditions. Using a parent stock of tirandamycin C in DMSO, serial dilutions were prepared to obtain stock solutions of varying concentrations of substrate for binding experiments. Purified P450s were diluted in storage buffer to a final concentration of 1 μM and transferred to a 1 cm quartz cuvette (Beckman). Varying concentrations of substrate were independently titrated into the solution in small aliquots (<2 μL) to achieve the desired final concentrations. Scans were recorded from 365 nm to 429 nm (2 nm steps) until the P450s became saturated. The starting spectrum was subtracted from subsequent experimental spectra and average absorbance differences ($\Delta A = A_{peak} - A_{trough}$) were plotted against concentration of substrate. The dissociation constant (K_d) for the P450s was calculated by fitting data points to either a nonlinear tight-binding quadratic equation (Equation 1) for high-affinity ligands (Kd ≤ 5 μM) or a rectangular hyperbolic function (Equation 2) for low-affinity ligands (Kd ≥ 5 μM) using the GraphPad Prism 8 software. All titrations were performed in triplicates and the K_d values reported represent the average of the three sets of data.

$$\Delta A = (A_{max} / 2[E]) (K_d + [E] + [S]) - (K_d + [E] + [S])^2 - 4 [E] [S]^{1/2} \quad \text{Equation 1}$$

$$\Delta A = A_{max} [S] / (K_d + [S]) \quad \text{Equation 2}$$

ΔA = Average absorbance difference (peak-to-trough) at each titration point; A_{max}= Maximum absorbance difference at substrate saturation; [E] = Total enzyme concentration; [S] = Substrate concentration

Enzyme assays:

Isolation of TirC has been described previously.[29] The *in vitro* enzymatic conversions of tirandamycins were performed in a total volume of 250 μl of conversion buffer (50 mM NaH_2PO_4, pH 7.4, 1 mM EDTA, 0.2 mM dithioerythritol, 10% glycerol) containing 500 μM substrates, 2 μM TamI, 4 mM spinach ferredoxin, 2 μM ferredoxin-$NADP^+$ reductase, 1mM $MgCl_2$, 5 mM glucose-6-phosphate, and 1 U/mL glucose-6-phosphate dehydrogenase in storage buffer (50 mM NaH_2PO_4, pH 7.4, 1 mM EDTA, 0.2 mM DTT, 10% (v/v) glycerol). Reactions were incubated at 30 °C (100 rpm) for 3h before quenching by extraction, using 2 × 200 ml of $CHCl_3$. The resulting organic extract was dried, redissolved in 120 ml of methanol and analyzed by the addition of 100 μL of methanol with HPLC. All reactions were performed and analyzed in triplicate. HPLC analysis was performed on an Agilent 1100 Series HPLC system with UV detection at 354 nm using a Phenomenex Luna C18 column with the following specifications: dimensions, 150 x 4.6 mm; particle size, 5 μm; pore size, 100 Å. For analysis of reactions HPLC conditions we used mobile phase (A = deionized water + 0.1% formic acid, B = acetonitrile + 0.1% formic acid); and the gradient 10% B for 1 min, 10% to 75% B over 35 min, 95% B for 1 min, 10% B for 2 min.

Computational Methods:

Quantum Mechanics: Conformational searches were performed with MMFF in Spartan. All QM calculations were performed with Gaussian 09.[40] Geometry optimizations and frequencies calculations were performed at the B3LYP level with LANL2DZ[41] for iron and 6-31 G(d) for all other atoms. Transition structures contained one negative frequency. Enthalpies and free energies were computed at 1 atm and 298.15K. A correction to the entropy was applied in accordance with the work of Truhlar et al.[42] Single point energy computations were performed at the B3LYP-D3(BJ) level with LANL2DZ for iron and 6-311+G(d,p) in gas phase for all calculations, except for the tetramic acid tautomer comparison, which included CPCM for water.

Molecular Dynamics (MD) Simulations: The heme iron(IV)-oxo complex involved in the cytochromecatalyzed oxidative hydroxyiation and epoxidation cycle (compound I) was used to model the active form of the cofactor. Simulations were performed using the GPU code (pmemd)[43] of the Amber 12 package,[44] The Amber-compatible parameters developed by Cheatham et al. were used for compound I and its axial Cys ligand.[45] Parameters for tirandamycin substrates were generated within the antechamber module using the general AMBER force field (gaff)[46], with partial charges set to fit the electrostatic potential

generated at the HF/6-31G(d) level by the RESP model.[47] The charges were calculated according to the Merz-Singh-Kollman[48-49] scheme using Gaussian 09. Each protein was immersed in a pre-equilibrated truncated cuboid box with a 10 Å buffer of TIP3P[50] water molecules using the tleap module, resulting in the addition of around 11370 solvent molecules. The systems were neutralized by addition of explicit counter ions (Na+ and Cl−). All subsequent calculations were done using the widely tested Stony Brook modification of the Amber 99 forced field (ff99sb).[46] The substrate and enzyme were optimized for total 1,000,000 steps, with 750,000 steepest descent steps and 250,000 conjugate gradient steps. The systems were gently heated using six 50 ps steps, incrementing the temperature by 50 K for each step (0-300 K) under constant-volume and periodic-boundary conditions. Water molecules were treated with the SHAKE algorithm such that the angle between hydrogen atoms were kept fixed. Long-range electrostatic effects were modelled using the particle-mesh-Ewald method.[51] An 8 Å cutoff was applied to the Lennard-Jones and electrostatic interactions. Harmonic restraints of 30kcal/(mol $Å^2$) were applied to the solute and the Andersen equilibration scheme was used to control and equalize the temperature. The time step was kept at 1 fs during the heating stages, allowing potential inhomogeneities to self-adjust. Each system was then equilibrated for 2 ns with a 2 fs time step at a constant volume. Production trajectories were then run for an additional 500 ns under the same simulation condtions.

Supplementary Material

Refer to Web version on PubMed Central for supplementary material.

Acknowledgements:

We are grateful to the National Science Foundation under the CCI Center for Selective C—H Functionalization (CHE-1700982), the National Institutes of Health (R35GM118101), and the Hans W. Vahlteich Professorship (to D.H.S.) for financial support.

References

1. Davies HM; Manning JR, Catalytic C—H functionalization by metal carbenoid and nitrenoid insertion. Nature 2008, 451 (7177), 417–24. [PubMed: 18216847]
2. Lamb DC; Follmer AH; Goldstone JV; Nelson DR; Warrilow AG; Price CL; True MY; Kelly SL; Poulos TL; Stegeman JJ, On the occurrence of cytochrome P450 in viruses. Proc Natl Acad Sci U S A 2019, 116 (25), 12343–12352. [PubMed: 31167942]
3. Rudolf JD; Chang CY; Ma M; Shen B, Cytochromes P450 for natural product biosynthesis in Streptomyces: sequence, structure, and function. Nat Prod Rep 2017, 34 (9), 1141–1172. [PubMed: 28758170]
4. Podust LM; Sherman DH, Diversity of P450 enzymes in the biosynthesis of natural products. Nat Prod Rep 2012, 29 (10), 1251–66. [PubMed: 22820933]
5. Girvan HM; Munro AW, Applications of microbial cytochrome P450 enzymes in biotechnology and synthetic biology. Curr Opin Chem Biol 2016, 31, 136–45. [PubMed: 27015292]
6. Zhang RK; Huang X; Arnold FH, Selective CH bond functionalization with engineered heme proteins: new tools to generate complexity. Curr Opin Chem Biol 2019, 49, 67–75. [PubMed: 30343008]
7. Brandenberg OF; Fasan R; Arnold FH, Exploiting and engineering hemoproteins for abiological carbene and nitrene transfer reactions. Curr Opin Biotechnol 2017, 47, 102–111. [PubMed: 28711855]

8. Hammer SC; Kubik G; Watkins E; Huang S; Minges H; Arnold FH, Anti-Markovnikov alkene oxidation by metal-oxo-mediated enzyme catalysis. Science 2017, 358 (6360), 215–218. [PubMed: 29026041]
9. Prier CK; Zhang RK; Buller AR; Brinkmann-Chen S; Arnold FH, Enantioselective, intermolecular benzylic C—H amination catalysed by an engineered iron-haem enzyme. Nat Chem 2017, 9 (7), 629–634. [PubMed: 28644476]
10. Dydio P; Key HM; Nazarenko A; Rha JY; Seyedkazemi V; Clark DS; Hartwig JF, An artificial metalloenzyme with the kinetics of native enzymes. Science 2016, 354 (6308), 102–106. [PubMed: 27846500]
11. Natoli SN; Hartwig JF, Noble-metal substitution in hemoproteins: an emerging strategy for abiological catalysis. Acc Chem Res 2019, 52 (2), 326–335. [PubMed: 30693758]
12. Carlson JC; Li S; Gunatilleke SS; Anzai Y; Burr DA; Podust LM; Sherman DH, Tirandamycin biosynthesis is mediated by co-dependent oxidative enzymes. Nat Chem 2011, 3 (8), 628–33. [PubMed: 21778983]
13. Reusser F, Tirandamycin, an inhibitor of bacterial ribonucleic acid polymerase. Antimicrob Agents Chemother 1976, 10 (4), 618–22. [PubMed: 791108]
14. Li S; Tietz DR; Rutaganira FU; Kells PM; Anzai Y; Kato F; Pochapsky TC; Sherman DH; Podust LM, Substrate recognition by the multifunctional cytochrome P450 MycG in mycinamicin hydroxylation and epoxidation reactions. J Biol Chem 2012, 287 (45), 37880–90. [PubMed: 22952225]
15. Zocher G; Richter ME; Mueller U; Hertweck C, Structural fine-tuning of a multifunctional cytochrome P450 monooxygenase. J Am Chem Soc 2011, 133 (7), 2292–302. [PubMed: 21280577]
16. McCormick SP; Alexander NJ; Proctor RH, *Fusarium* Tri4 encodes a multifunctional oxygenase required for trichothecene biosynthesis. Can J Microbiol 2006, 52 (7), 636–42. [PubMed: 16917519]
17. Morrone D; Chen XM; Coates RM; Peters RJ, Characterization of the kaurene oxidase CYP701A3, a multifunctional cytochrome P450 from gibberellin biosynthesis. Biochem J 2010, 431, 337–344. [PubMed: 20698828]
18. Sherman DH; Li S; Yermalitskaya LV; Kim Y; Smith JA; Waterman MR; Podust LM, The structural basis for substrate anchoring, active site selectivity, and product formation by P450 PikC from *Streptomyces venezuelae*. J Biol Chem 2006, 281 (36), 26289–97. [PubMed: 16825192]
19. Holm L; Rosenstrom P, Dali server: conservation mapping in 3D. Nucleic Acids Res 2010, 38 (Web Server issue), W545–9. [PubMed: 20457744]
20. Jozwik IK; Litzenburger M; Khatri Y; Schifrin A; Girhard M; Urlacher V; Thunnissen AWH; Bernhardt R, Structural insights into oxidation of medium-chain fatty acids and flavanone by myxobacterial cytochrome P450 CYP267B1. Biochem J 2018, 475 (17), 2801–2817. [PubMed: 30045877]
21. Herzog K; Bracco P; Onoda A; Hayashi T; Hoffmann K; Schallmey A, Enzyme-substrate complex structures of CYP154C5 shed light on its mode of highly selective steroid hydroxylation. Acta Crystallogr D Biol Crystallogr 2014, 70 (Pt 11), 2875–89. [PubMed: 25372679]
22. Makino M; Sugimoto H; Shiro Y; Asamizu S; Onaka H; Nagano S, Crystal structures and catalytic mechanism of cytochrome P450 StaP that produces the indolocarbazole skeleton. Proc Natl Acad Sci U S A 2007, 104 (28), 11591–6. [PubMed: 17606921]
23. Du L; Dong S; Zhang X; Jiang C; Chen J; Yao L; Wang X; Wan X; Liu X; Wang X; Huang S; Cui Q; Feng Y; Liu SJ; Li S, Selective oxidation of aliphatic C—H bonds in alkylphenols by a chemomimetic biocatalytic system. Proc Natl Acad Sci U S A 2017, 114 (26), E5129–E5137. [PubMed: 28607077]
24. Nagano S; Poulos TL, Crystallographic study on the dioxygen complex of wild-type and mutant cytochrome P450cam. Implications for the dioxygen activation mechanism. J Biol Chem 2005, 280 (36), 31659–63. [PubMed: 15994329]
25. Li S; Chaulagain MR; Knauff AR; Podust LM; Montgomery J; Sherman DH, Selective oxidation of carbolide C—H bonds by an engineered macrolide P450 mono-oxygenase. Proc Natl Acad Sci U S A 2009, 106 (44), 18463–8. [PubMed: 19833867]

26. Narayan AR; Jimenez-Oses G; Liu P; Negretti S; Zhao W; Gilbert MM; Ramabhadran RO; Yang YF; Furan LR; Li Z; Podust LM; Montgomery J; Houk KN; Sherman DH, Enzymatic hydroxylation of an unactivated methylene C—H bond guided by molecular dynamics simulations. Nat Chem 2015, 7 (8), 653–60. [PubMed: 26201742]
27. DeMars MD 2nd; Sheng F; Park SR; Lowell AN; Podust LM; Sherman DH, Biochemical and structural characterization of MycCI, a versatile P450 biocatalyst from the mycinamicin biosynthetic pathway. ACS Chem Biol 2016, 11 (9), 2642–54. [PubMed: 27420774]
28. DeMars MD 2nd; Samora NL; Yang S; Garcia-Borras M; Sanders JN; Houk KN; Podust LM; Sherman DH, Exploring the molecular basis for substrate specificity in homologous macrolide biosynthetic cytochromes P450. J Biol Chem 2019, 294 (44), 15947–15961. [PubMed: 31488542]
29. Carlson JC; Li S; Burr DA; Sherman DH, Isolation and characterization of tirandamycins from a marine-derived *Streptomyces* sp. J Nat Prod 2009, 72 (11), 2076–9. [PubMed: 19883065]
30. Inoue H; Nojima H; Okayama H, High efficiency transformation of *Escherichia coli* with plasmids. Gene 1990, 96 (1), 23–8. [PubMed: 2265755]
31. Omura T; Sato R, The carbon monoxide-binding pigment of liver microsomes. I. evidence for its hemoprotein nature. J Biol Chem 1964, 239, 2370–8. [PubMed: 14209971]
32. Zhang W; Liu Y; Yan JY; Cao SN; Bai FL; Yang Y; Huang SH; Yao LS; Anzai Y; Kato F; Podust LM; Sherman DH; Li SY, New reactions and products resulting from alternative interactions between the P450 enzyme and redox partners. J Am Chem Soc 2014, 136 (9), 3640–3646. [PubMed: 24521145]
33. Battye TG; Kontogiannis L; Johnson O; Powell HR; Leslie AG, iMOSFLM: a new graphical interface for diffraction-image processing with MOSFLM. Acta Crystallogr D Biol Crystallogr 2011, 67 (Pt 4), 271–81. [PubMed: 21460445]
34. Collaborative Computational Project N, The CCP4 suite: programs for protein crystallography. Acta Crystallogr D Biol Crystallogr 1994, 50 (Pt 5), 760–3. [PubMed: 15299374]
35. McCoy AJ; Grosse-Kunstleve RW; Adams PD; Winn MD; Storoni LC; Read RJ, Phaser crystallographic software. J Appl Crystallogr 2007, 40 (Pt 4), 658–674. [PubMed: 19461840]
36. Emsley P; Cowtan K, Coot: model-building tools for molecular graphics. Acta Crystallogr D Biol Crystallogr 2004, 60 (Pt 12 Pt 1), 2126–32. [PubMed: 15572765]
37. Murshudov GN; Skubak P; Lebedev AA; Pannu NS; Steiner RA; Nicholls RA; Winn MD; Long F; Vagin AA, REFMAC5 for the refinement of macromolecular crystal structures. Acta Crystallogr D Biol Crystallogr 2011, 67 (Pt 4), 355–67. [PubMed: 21460454]
38. Adams PD; Afonine PV; Bunkoczi G; Chen VB; Davis IW; Echols N; Headd JJ; Hung LW; Kapral GJ; Grosse-Kunstleve RW; McCoy AJ; Moriarty NW; Oeffner R; Read RJ; Richardson DC; Richardson JS; Terwilliger TC; Zwart PH, PHENIX: a comprehensive Python-based system for macromolecular structure solution. Acta Crystallogr D Biol Crystallogr 2010, 66 (Pt 2), 213–21. [PubMed: 20124702]
39. Kabsch W, Xds. Acta Crystallogr D Biol Crystallogr 2010, 66 (Pt 2), 125–32. [PubMed: 20124692]
40. Frisch MJ, T. GWSchlegel HB, Scuseria GE, Robb MA, Cheeseman JR, Scalmani G, Barone V, Petersson GA, Nakatsuji H, Li X, Caricato M, Marenich A, Bloino J, Janesko BG, Gomperts R, Mennucci B, Hratchian HP, Ortiz JV, Izmaylov AF, Sonnenberg JL, Williams-Young D, Ding F, Lipparini F, Egidi F, Goings J, Peng B, Petrone A, Henderson T, Ranasinghe D, Zakrzewski VG, Gao J, Rega N, Zheng G, Liang W, Hada M, Ehara M, Toyota K, Fukuda R, Hasegawa J, Ishida M, Nakajima T, Honda Y, Kitao O, Nakai H, Vreven T, Throssell K, Montgomery JA Jr., Peralta JE, Ogliaro F, Bearpark M, Heyd JJ, Brothers E, Kudin KN, Staroverov VN, Keith T, Kobayashi R, Normand J, Raghavachari K, Rendell A, Burant JC, Iyengar SS, Tomasi J, Cossi M, Millam JM, Klene M, Adamo C, Cammi R, Ochterski JW, Martin RL, Morokuma K, Farkas O, Foresman JB, and Fox DJ, Gaussian 09, Revision A. 02. Gaussian. Inc.: Wallingford, CT 2009.
41. Hay PJ; Wadt WR, *Ab initio* effective core potentials for molecular calculations - potentials for the transition-metal atoms Sc to Hg. J Chem Phys 1985, 82 (1), 270–283.
42. Zhao Y; Truhlar DG, The M06 suite of density functionals for main group thermochemistry, thermochemical kinetics, noncovalent interactions, excited states, and transition elements: two new

functionals and systematic testing of four M06-class functionals and 12 other functionals. Theor Chem Acc 2008, 120 (1-3), 215–241.

43. Salomon-Ferrer R; Gotz AW; Poole D; Le Grand S; Walker RC, Routine microsecond molecular dynamics simulations with AMBER on GPUs. 2. explicit solvent particle mesh Ewald. J Chem Theory Comput 2013, 9 (9), 3878–3888. [PubMed: 26592383]
44. Case DA, AMBER 12 (UCSF, 2012).
45. Shahrokh K; Orendt A; Yost GS; Cheatham TE 3rd, Quantum mechanically derived AMBER-compatible heme parameters for various states of the cytochrome P450 catalytic cycle. J Comput Chem 2012, 33 (2), 119–33. [PubMed: 21997754]
46. Wang J; Wolf RM; Caldwell JW; Kollman PA; Case DA, Development and testing of a general amber force field. J Comput Chem 2004, 25 (9), 1157–74. [PubMed: 15116359]
47. Bayly CI; Cieplak P; Cornell WD; Kollman PA, A well-behaved electrostatic potential based method using charge restraints for deriving atomic charges - the resp model. J Phys Chem-Us 1993, 97 (40), 10269–10280.
48. Besler BH; Merz KM; Kollman PA, Atomic charges derived from semiempirical methods. J Comput Chem 1990, 11 (4), 431–439.
49. Singh UC; Kollman PA, An approach to computing electrostatic charges for molecules. J Comput Chem 1984, 5 (2), 129–145.
50. Jorgensen WL; Chandrasekhar J; Madura JD; Impey RW; Klein ML, Comparison of simple potential functions for simulating liquid water. J Chem Phys 1983, 79 (2), 926–935.
51. Darden T; York D; Pedersen L, Particle mesh Ewald: An N·log(N) method for Ewald sums in large systems. J Chem Phys 1993, 98 (12), 10089–10092.

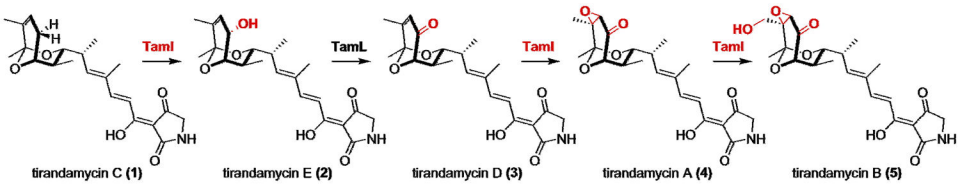

Figure 1. TamI oxidations.

TamI catalyzes iterative oxidation of bicyclic ketal of **1**. The C10 hydroxyl of **2** is oxidized to a ketone by the TamL flavoprotein.

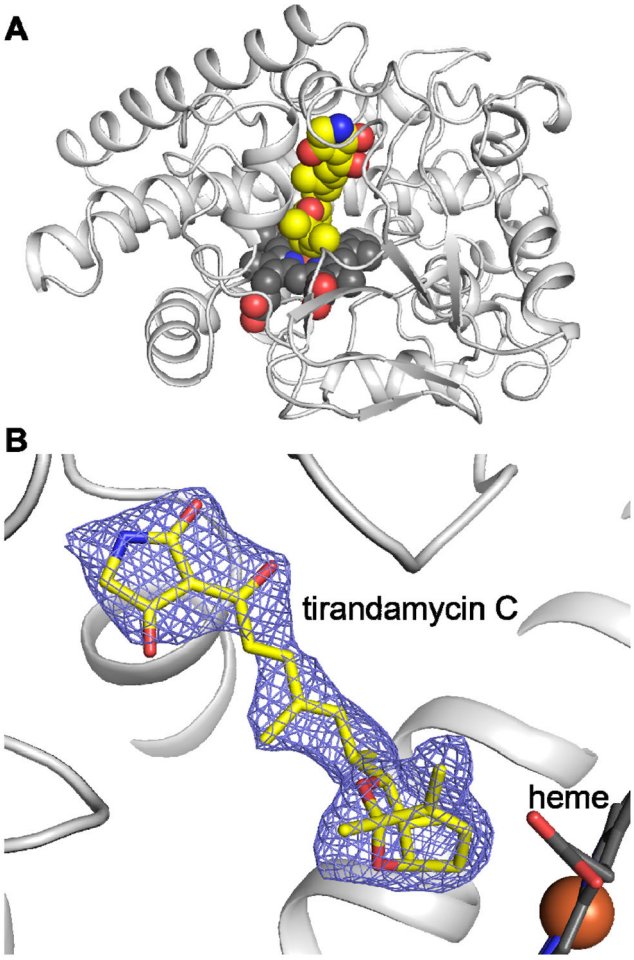

Figure 2. Structure of TamI in complex with 1.

(A) Cartoon representation of the complex. **1** is shown in yellow space-filling model; heme is shown in black. (B) Omit map (Fo-Fc) for **1**. The bicyclic ketal is proximal to the heme.

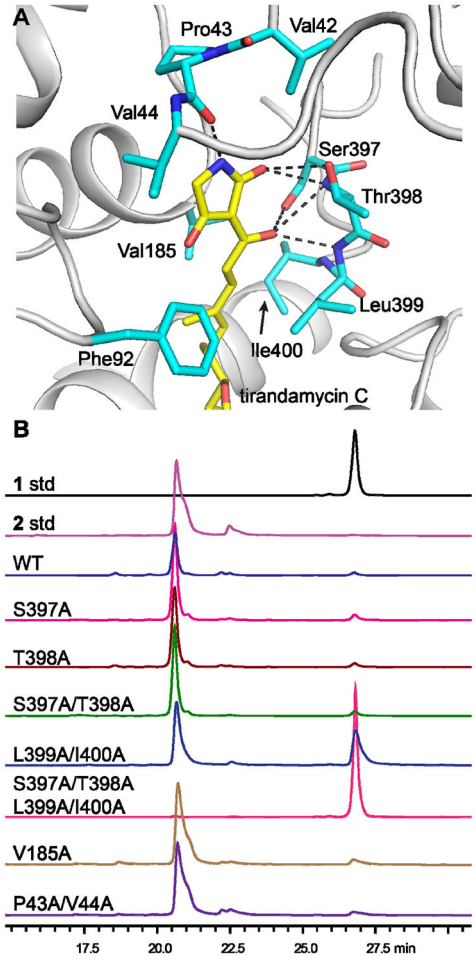

Figure 3. Tetramic acid binding site.

(A) Stick representation of key contacts proximal to tetramic acid. (B) HPLC traces for endpoint assays with TamI mutants. Signal is UV absorbance at 340 nm. **2** shows peak shoulder due to tautomerization in methanol.

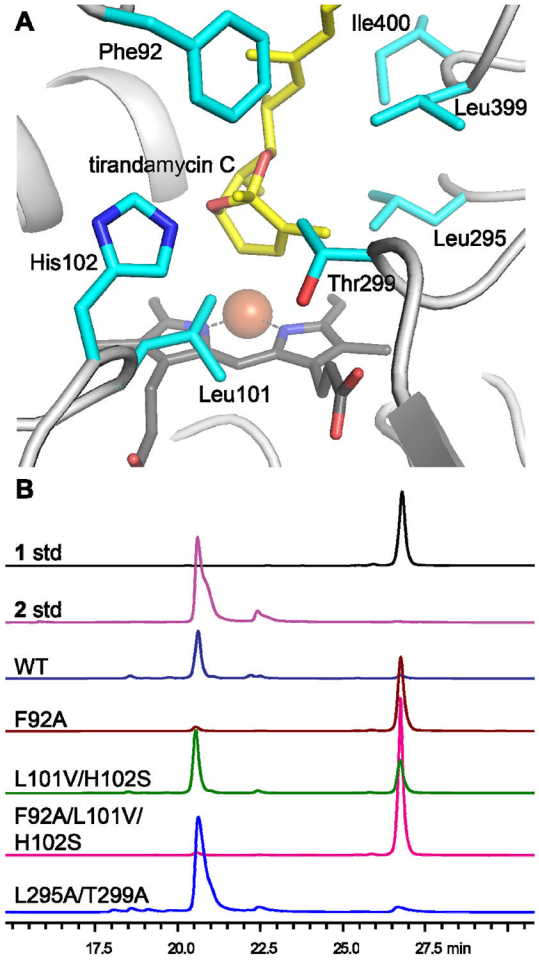

Figure 4. Bicyclic ketal binding site.

(A) Stick representation of key contacts proximal to the tirandamycin bicyclic ketal. (B) HPLC traces for endpoint assays with TamI mutants. Signal is UV absorbance at 340 nm. **2** shows peak shoulder due to tautomerization in methanol.

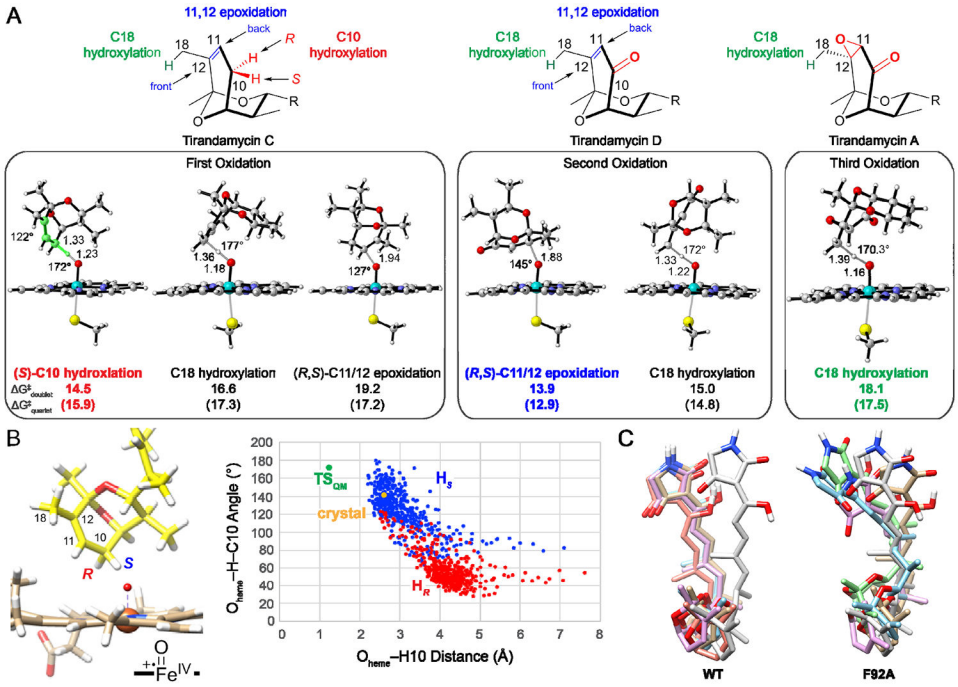

Figure 5. Computational analysis of TamI iterative oxidation.

(A) Intrinsic energy for each of the three oxidation steps in tirandamycin biosynthesis. (B) MD simulations showing TamI interaction with **1**. The pro-S hydrogen resides closer to the QM ideal transition state (green dot) geometry in the crystal structure (orange dot) and throughout the simulation. (C) Overlays of top five occupied clusters for **1** with WT and F92A TamI.

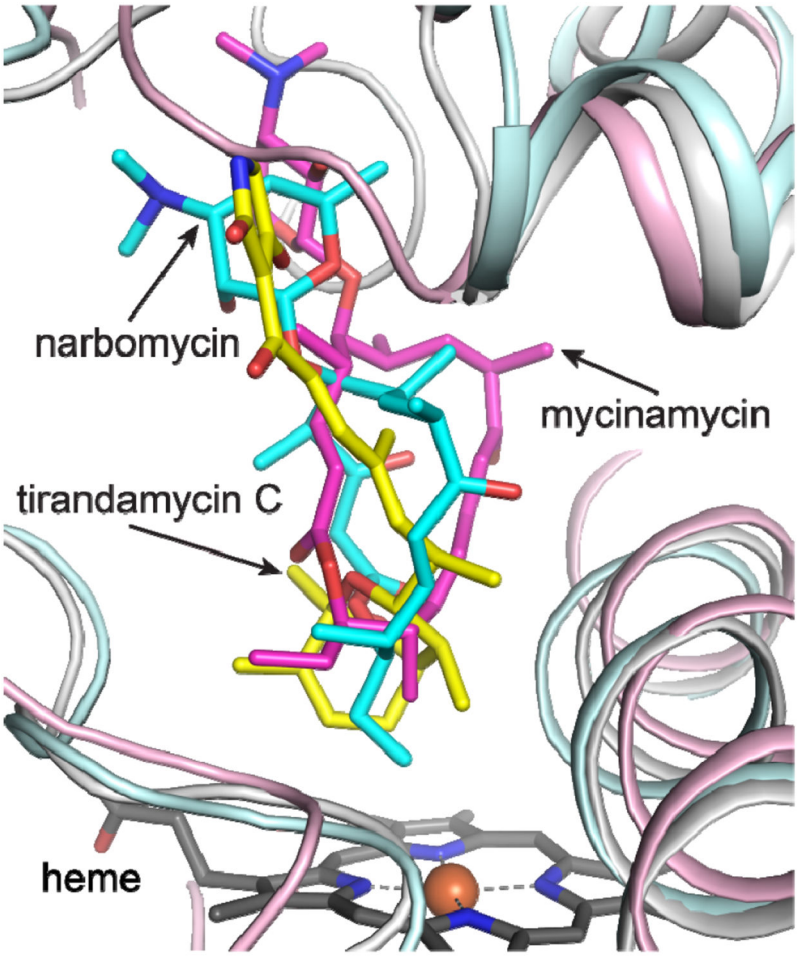

Figure 6. Overlay of TamI with PikC ana MycCI.

Despite the evident similarity in binding mode of their respective substrates, different factors drive molecular recognition in TamI (gray) compared to PikC (cyan, 2C7X) and MycCI (magenta, 5FOI). **1** is colored yellow.